

Spontaneous time-reversal symmetry breaking in twisted double bilayer graphene

Received: 14 April 2022

Accepted: 12 October 2022

Published online: 29 October 2022

 Check for updates

Manabendra Kuri ¹✉, Christopher Coleman ¹, Zhenxiang Gao¹,
Aswin Vishnuradhan¹, Kenji Watanabe ², Takashi Taniguchi ³, Jihang Zhu⁴,
Allan H. MacDonald ⁴ & Joshua Folk ¹✉

Twisted double bilayer graphene (tDBG) comprises two Bernal-stacked bilayer graphene sheets with a twist between them. Gate voltages applied to top and back gates of a tDBG device tune both the flatness and topology of the electronic bands, enabling an unusual level of experimental control. Metallic states with broken spin and valley symmetries have been observed in tDBG devices with twist angles in the range 1.2–1.3°, but the topologies and order parameters of these states have remained unclear. We report the observation of an anomalous Hall effect in the correlated metal state of tDBG, with hysteresis loops spanning hundreds of mT in out-of-plane magnetic field (B_{\perp}) that demonstrate spontaneously broken time-reversal symmetry. The B_{\perp} hysteresis persists for in-plane fields up to several Tesla, suggesting valley (orbital) ferromagnetism. At the same time, the resistivity is strongly affected by even mT-scale values of in-plane magnetic field, pointing to spin-valley coupling or to a direct orbital coupling between in-plane field and the valley degree of freedom.

The interplay between band topology and Coulomb interactions has emerged as a frontier in the study of two-dimensional (2D) materials with flat electronic bands^{1–5}. Graphene-based van der Waals (vdW) heterostructures offer a flexible platform from which to investigate this interplay, due to their native Dirac points close to the Fermi level that provide a resource for band topology. Flat bands may be engineered by clever heterostructure design^{1,2,6} and tuned using experimental knobs such as magnetic field or gate voltage^{7,8}; the topology of the resulting bands is then readily controlled, whether by choice of heterostructure stacking or by tuning applied gate voltages^{9,10}. Starting from flat bands, Coulomb interactions often lead to spontaneous symmetry breaking, yielding exotic electronic phases such as fractional Chern insulators¹¹ or unconventional superconductivity^{2,12}.

The physical phenomenology that results from broken symmetry phases depends on the topology of the underlying electronic bands^{5,13}. For example, the anomalous Hall effect (AHE) is a striking experimental

signature that emerges due to spontaneously broken time reversal symmetry associated with spin or valley polarization. This broken time reversal symmetry creates an “anomalous” Hall resistivity when transport is via bands with finite Berry curvature¹⁴. AHE reflecting orbital ferromagnetism has been reported in multi-layer vdW heterostructures such as twisted bilayer graphene aligned with hexagonal boron nitride (*h*BN)^{15,16}, and in naturally-occurring structures like Bernal-stacked (AB) bilayer graphene¹⁷.

Twisted double bilayer graphene (tDBG)—two AB-stacked bilayer graphene sheets misaligned by twist angle θ —is a uniquely tunable system in which band topology, correlations and broken symmetry phases can be manipulated using top- and back-gate voltages to control the electrostatic doping, n , and vertical displacement field, D (Fig. 1a)^{9,10,18}. When $\theta = 1.3^{\circ}$, the moiré-modified conduction band (hereafter referred to as the moiré band) can be tuned using D to be nearly flat, separated from a dispersive band at higher energy and from

¹Department of Physics and Astronomy & Stewart Blusson Quantum Matter Institute, University of British Columbia, Vancouver, BC V6T 1Z4, Canada.

²Research Center for Functional Materials, National Institute for Materials Science, Namiki 1-1, Tsukuba, Ibaraki 305-0044, Japan. ³International Center for Materials Nanoarchitectonics, National Institute for Materials Science, Namiki 1-1, Tsukuba, Ibaraki, Japan. ⁴Physics Department, University of Texas at Austin, Austin, TX 78712, USA. ✉ e-mail: koolmanab@gmail.com; jfolk@physics.ubc.ca

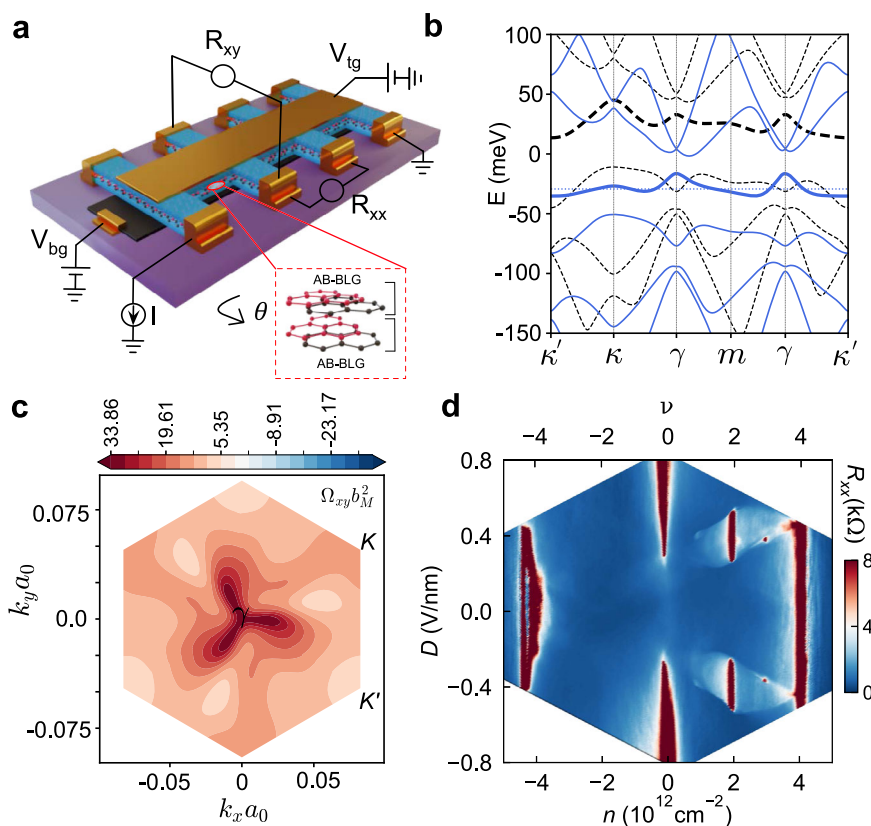


Fig. 1 | Twisted double bilayer graphene. **a** Schematic of a tDBG device consisting of two Bernal (AB) bilayer graphene layers stacked with a twist angle $\theta \approx 1.3^\circ$. The stack is encapsulated with top and bottom hexagonal boron nitride (hBN) layers, with a graphite bottom-gate (V_{bg}) and a metal top-gate (V_{tg}) to independently tune the density (n) and displacement field (D). **b** Calculated moiré band dispersion for tDBG with twist

angle $\theta = 1.3^\circ$ and $D = 0.44$ V/nm. The solid (dashed) line corresponds to Hartree-Fock (single particle) calculations, with thicker lines indicating the first conduction band. HF calculations are filling-dependent, and are made for $\nu = 3.7$. **c** Berry curvature (Ω) calculated for the conduction band. **d** Four terminal resistance, R_{xx} , as a function of n and D at $T = 20$ mK, $B = 0$ for D1. The top axis shows the band filling, ν .

the valence band below (Fig. 1b)¹⁹. For gate voltages that place the Fermi energy within such a flat and isolated moiré band, transport measurements typically report regions of higher resistivity sometimes referred to as ‘haloes’. Theoretical predictions^{9,10,20} and experimental data^{19,21–28} indicate that, within the halo regions, the moiré band is topologically non-trivial and interactions lead to broken spin and valley symmetries, similar to the symmetry breaking observed in quantum Hall ferromagnetism^{29,30}.

The precise way in which spin and valley symmetries are broken in tDBG remains an open problem^{10,19,21,24}. Valley-polarized, spin-valley-locked, spin-polarized, and intervalley coherent states have all been considered¹⁰. The consistent observation of an insulating state when the moiré band is half filled provides a valuable clue. The resistance of this state increases with in-plane field, B_{\parallel} , suggesting that the metallic states on either side may be spin polarized^{21,22,24} but leaving the question of possible valley order unaddressed^{19,24,31}. In particular, an AHE of the kind reported in other graphene systems has not been reported in tDBG with small θ .

Here, we report the observation of a strong AHE in AB-AB stacked tDBG ($\theta = 1.3^\circ$), with longitudinal (R_{xx}) and Hall resistance (R_{xy}) that are sharply hysteretic under out-of-plane magnetic field (B_{\perp}). The data demonstrate orbital (valley) time reversal symmetry breaking, which modifies the Hall resistivity when there is strong Berry curvature¹⁴, confirming predictions for tDBG near the top of the moiré band (Fig. 1c). Qualitative differences between in- and out-of-plane magnetic field dependence in the AHE signatures reinforce the orbital (valley) character of the ferromagnetism^{32,33}. At the same time, both longitudinal and transverse resistivity are sensitive to unusually small in-plane magnetic fields, an effect that is not yet understood.

Results

Devices were fabricated using established techniques^{1,34} (see Methods), and patterned into Hall bar geometries to measure R_{xx} and R_{xy} . Figure 1a shows a schematic of the device architecture and measurement scheme. Multiple voltage probe pairs were measured in each device, with similar behaviour across most pairs (see SI). Mixing between R_{xx} and R_{xy} has been minimized in the data as presented by reporting the field symmetrized longitudinal resistance, henceforth labelled ρ_{xx} , and the anti-symmetrized transverse resistance, ρ_{xy} (see Methods). Reported values of B_{\perp} have been adjusted to reflect flux trapping in the superconducting magnet (see SI). Similar behaviour is seen in two devices (D1 and D2), with twist angles $\theta \approx 1.31^\circ$ and $\theta \approx 1.34^\circ$ respectively; these were the only two devices with twist angle near 1.3° that were measured.

A typical resistivity map over top- and back-gate is shown in Fig. 1d, plotted with respect to n and D . Insulating stripes at $n = 0$ reflect the separation of conduction from valence band by finite D , while the insulating stripe around $n = 4 \times 10^{12} \text{ cm}^{-2}$ reflects full filling of the first conduction band. Given the 4-fold degeneracy of the band (spin and valley), full filling is achieved at four electrons per moiré cell ($\nu = 4$), allowing the twist angle to be calculated and the relation between n and ν determined (see Methods). Near $D = \pm 0.4$ V/nm, numerical calculations indicate a moiré band that is nearly flat and isolated both from lower and upper bands. Figure 1b shows single-particle and self-consistent Hartree calculations of the moiré band structure for the parameters matching experimental conditions (see caption), illustrating the flatness of the band especially in the self-consistent calculation that highlights the role of interactions^{19,35}.

Setting D near ± 0.4 V/nm in the device, a strong insulating state at $\nu = 2$ is clearly visible, consistent with previous reports^{21,22,24}, with

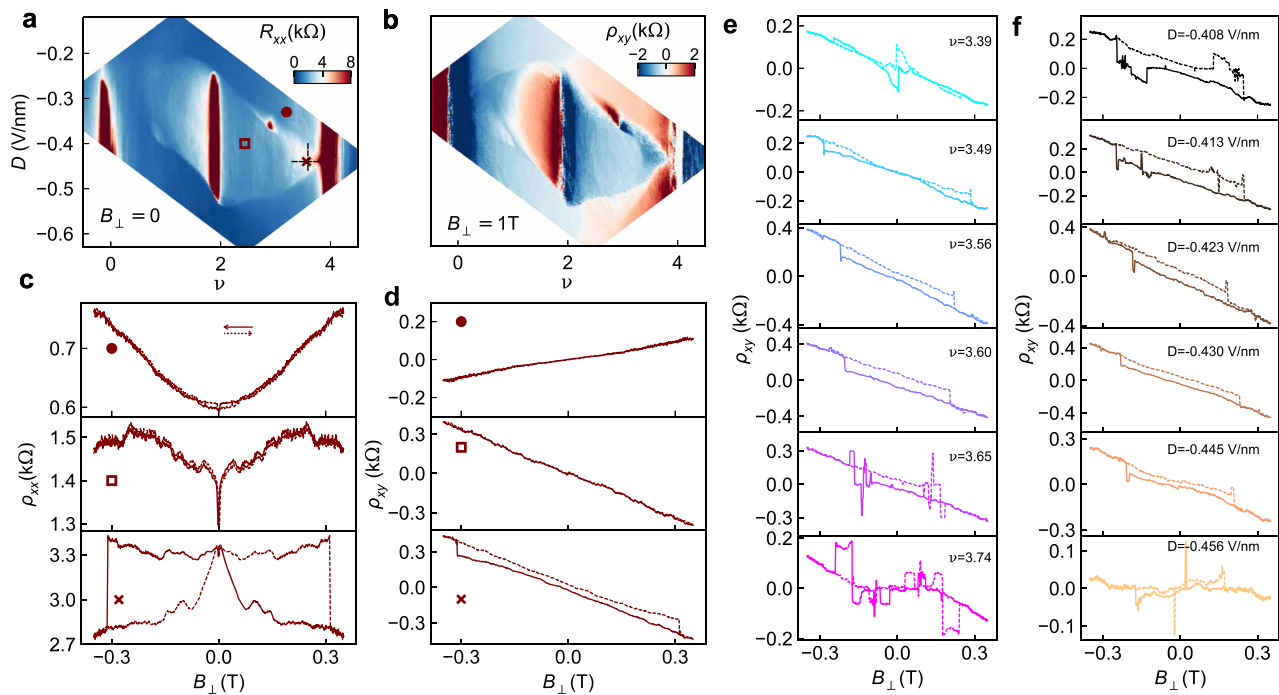


Fig. 2 | Out-of-plane magnetoresistance. **a** R_{xx} as function of ν and D showing the correlated insulating states at $\nu=2$ and $\nu=3$, appearing in red by the colour scale chosen here, surrounded by a halo region that is metallic but higher resistance (light blue) than the surrounding areas (dark blue). **b** Anti-symmetrized Hall resistance, ρ_{xy} , for $|B_{\perp}|=1$ T. The Hall resistance changes sign at integer fillings and also at the boundary of the halo region. **c, d** Magnetic field dependence of the

symmetrized longitudinal resistance, $\rho_{xx}(B_{\perp})$, and anti-symmetrized Hall resistance, $\rho_{xy}(B_{\perp})$, for three values of $\{\nu, D\}$ marked in **a**. B_{\perp} is swept back and forth, shown with solid (positive to negative) and dashed (negative to positive) lines. **e, f** $\rho_{xy}(B_{\perp})$ as B_{\perp} is swept back and forth (solid/dashed) for (e) varying fillings $\nu=3.4 \rightarrow 3.75$ at fixed $D=-0.43$ V/nm, and (f) varying $D=-0.4 \rightarrow -0.46$ V/nm at fixed $\nu=3.6$. D1 at $T=20$ mK for all.

surrounding 'halo' regions of higher resistivity sharply separated from a lower-resistance background. The relatively narrow range of $|D|$ over which the halos appear is explained by the importance of an isolated narrow band for strong interaction effects: at too-small values of $|D|$ there is almost no gap between conduction and valence band, while for too-large D the first moiré band overlaps with the second. The high quality of these devices is demonstrated by the the strong insulating state at $\nu=3$ even at $\mathbf{B}=0$; this signature is known to emerge only over a narrow range of twist angle $\theta \sim 1.3^{\circ}$ ²⁴ where the correlations are maximum.

Figure 2a offers a higher resolution map of R_{xx} across the halo region at negative D , with insulating states at $\nu=2$ and $\nu=3$ clearly visible. More insight into the broken-symmetry metallic states within the halo may be obtained from the Hall resistance, shown for $B_{\perp}=\pm 1$ T in Fig. 2b. ρ_{xy} changes sign across $\nu=2$ within the entire halo, and also at $\nu=3$ across a narrow region at the low- D edge of the halo. This behaviour implies that the 4-fold band degeneracy is broken throughout the halo region, and fully lifted for a narrow range of D .

The most telling data comes from the magnetoresistance of the correlated metallic states. Figure 2c, d show ρ_{xx} and ρ_{xy} as B_{\perp} is swept from 350 mT to -350 mT and back, comparing data for three $\{\nu, D\}$ pairs, indicated by markers in Fig. 2a. These datasets are chosen to illustrate three characteristic behaviours observed within the $\{\nu, D\}$ map. Outside the halo region (\bullet), longitudinal magnetoresistance is weak and the data are independent of sweep direction, consistent with the behaviour of non-interacting metals. Within the halo but far from $\nu=4$ (\square), ρ_{xx} shows an additional strong but narrow positive magnetoresistance, but ρ_{xy} is again nearly linear and neither $\rho_{xx}(B_{\perp})$ nor $\rho_{xy}(B_{\perp})$ depend on sweep direction. Within the halo and near $\nu=4$ (\times), both ρ_{xy} and ρ_{xx} are reversly hysteretic, a clear indication of spontaneously broken time reversal symmetry giving rise to ferromagnetism with coercive fields near 0.3 T (bottom panels in Fig. 2c,d). AHE was also observed for the halo at positive D , though the hysteresis was less pronounced (see SI).

The range of ν over which ferromagnetic AHE signals appear is illustrated in Fig. 2e, showing data along the $D=-0.43$ V/nm line in Fig. 2a. Close to the single-particle insulator ($\nu > 3.75$), multiple jumps are seen in up-and-down magnetic field sweeps, indicating multi-domain switching behaviour; this behaviour continues deep into the insulating state. Throughout the range $3.5 \lesssim \nu \lesssim 3.7$, the hysteresis loop was wide and clean with nearly constant coercive field, then below $\nu \sim 3.4$ both the width and height of the hysteresis loop collapsed. The reduced width of the loops indicates lower coercive fields for $\nu \lesssim 3.4$. The reduced height may result from reduced valley polarization or smaller Berry curvature: numerical calculations indicate that the strongest Berry curvature is near $k_x=k_y=0$, corresponding to the highest energy (last-filled) states in the moiré band (Fig. 1c). For $\nu < 3.3$, no R_{xy} hysteresis loops of the form shown in Fig. 2d, f were seen, though evidence of first-order domain flips was visible in the narrow region of gate voltage immediately adjacent to the $\nu=3$ insulating state (see SI). Taken together, the data are consistent with valley polarization originating from the $\nu=3$ state but only developing into AHE with strong Berry curvature above $\nu=3.4$.

Interestingly, AHE hysteresis loops were nearly independent of D within the halo, although outside the halo they were absent. The data in Fig. 2f represent the evolution of the AHE at fixed $\nu=3.6$, varying the displacement field from $D=-0.4$ V/nm to $D=-0.46$ V/nm (Fig. 2f). This uniformity contrasts with the very narrow range of D over which the $\nu=3$ insulating state is observed.

Having established a ferromagnetic AHE close to full filling of the moiré band, we turn to the question of whether spin or valley symmetry breaking is responsible for the observed effect. Previous reports of spin polarization in the $\nu=2$ insulator and presumably in the surrounding metallic states might suggest spin ferromagnetism as a possible source for the AHE, but the weak spin-orbit interaction³⁶ of graphene makes this explanation less likely. Experimental input into

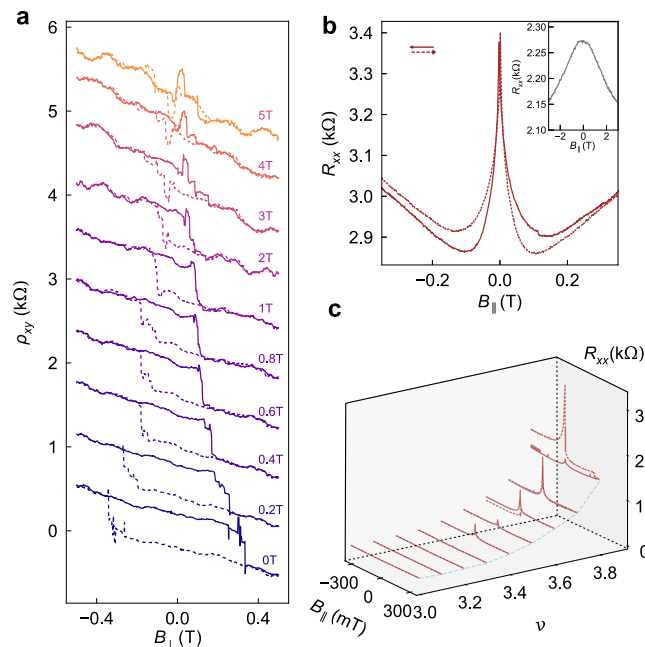


Fig. 3 | Anisotropic magnetoresistance. **a** Hysteresis in $\rho_{xy}(B_{\perp})$ for fixed in-plane magnetic fields (B_{\parallel}) up to 5 T. The curves are offset by 600 Ω for clarity (D2, $\nu = 3.57$, $D = -0.43$ V/nm, $T = 100$ mK). **b** A sharp peak in $R_{xx}(B_{\parallel})$ is observed at $B_{\parallel} = 0$ throughout the AHE region. The slight offset in R_{xx} , comparing up and down traces away from $B = 0$, is caused by additional heating of the sample when sweeping the magnet away from zero field. Inset: finer scan just over the peak illustrates rounding on the $B_{\parallel} = 1$ mT field scale (D1, $\nu = 3.43$, $D = -0.42$ V/nm, $T = 100$ mK). **c** Evolution of the $R_{xx}(B_{\parallel})$ magnetoresistance with ν . The peak appears immediately upon entering the AHE region ($\nu \geq 3.4$). Difference between up and down traces illustrates irreproducibility of B_{\parallel} sweeps at low field (D2, $D = -0.43$ V/nm, $T = 300$ mK, $B_{\perp} = 0$).

this question is obtained from a comparison of in-plane and out-of-plane magnetoresistance: whereas the valley degree of freedom couples primarily to out-of-plane field, spins are expected to couple to total magnetic field with $g = -2$.

Figure 3 explores the effect of B_{\parallel} in more detail. A clear illustration of the anisotropic nature of the AHE comes from Fig. 3a, where B_{\perp} hysteresis loops (± 450 mT) are shown for increasing fixed B_{\parallel} . A particularly robust AHE in D2 exhibits a small hysteresis loop in B_{\perp} , with coercive field around ~ 50 mT, even when B_{\parallel} is held at 5T. (Equivalent data for D1 show B_{\perp} hysteresis persisting above $B_{\parallel} \sim 1$ T, see SI.) The weak dependence of the AHE on the in-plane component of the magnetic field, up to B_{\parallel} of several Tesla, is reminiscent of the angle-dependent hysteretic AHE observed in twisted bilayer graphene aligned to $h\text{BN}$ ³³. In that work, the AHE signal depended exclusively on the out-of-plane magnetic field component, leading to the conclusion that the AHE signal must be attributed to valley polarization. That conclusion was based on the understanding that valley order is only weakly sensitive to B_{\parallel} .

Discussion

In our measurements of tDBG, as in ref. 33, there is a qualitative distinction between phenomena driven by B_{\perp} and B_{\parallel} . But the influence of B_{\parallel} is nevertheless very strong—much stronger (especially for small B_{\parallel}) than in ref. 33. Figure 3b, c provide illustrations of this extreme B_{\parallel} magnetoresistance, which was observed in both devices. Throughout the AHE region an anomalously sharp negative B_{\parallel} -magnetoresistance was observed (Fig. 3b), with a rounding around zero field on the $B_{\parallel} \sim 1$ mT scale that is orders of magnitude smaller than what might be expected when comparing $g\mu_B B_{\parallel}$ to $k_B T$ ($k_B T/g\mu_B \sim 100$ mT at 100 mK for $g = 2$). Examining a sequence of B_{\parallel} sweeps for increasing ν , along a

line of fixed $D = -0.43$ in the centre of the halo (Fig. 3c, c.f. Fig. 2e), the peak appears immediately upon entering the AHE region ($\nu \geq 3.4$) and grows with larger values of ν . Beyond the consistently-observed peak in $R_{xx}(B_{\parallel})$, however, the details of B_{\parallel} magnetoresistance in the AHE region were less repeatable from scan to scan than the hysteresis in B_{\perp} that is the primary subject of this work. The B_{\parallel} scans in Fig. 3c are neither hysteretic nor exactly reproducible, in marked contrast to the AHE hysteresis loops reported elsewhere in this work, which retrace scan after scan.

The striking effects of small B_{\parallel} seen in Fig. 3 have not, to our knowledge, been reported before; they appear in both devices, and only inside the AHE regions. These effects may be due to the coupling, albeit weak, of B_{\parallel} to valley order¹⁰. Even though this coupling is small, proportional to the thickness of the double bilayer, it competes with a valley anisotropy that is poorly understood at present and likely also to be weak. Alternately, B_{\parallel} could influence the AHE via spin-orbit coupling as reported recently in twisted (single) bilayer graphene with spin-orbit interaction enhanced by proximity to WSe_2 ³⁷. Although spin-orbit coupling was not intentionally enhanced in our devices, this possibility cannot be excluded. A more complete study of the B_{\parallel} -induced effects in tDBG will be the subject of future work.

The AHE signatures seen in Fig. 2 persist up to 1.8 K in D2 (similar in D1), illustrating the relatively large energy scales associated with valley symmetry breaking in this system. Figure 4a, b show the temperature-induced collapse of the hysteresis loop via shrinking coercive field for ρ_{xy} and ρ_{xx} respectively. Early measurements of tDBG noted a step-like rise in R_{xx} with temperature within the halo region, which has been attributed to temperature-induced collapse of broken symmetry states²⁴. An analogous rise in R_{xx} around 7 K is observed in our measurements away from the AHE region ($\nu < 3.2$, Fig. 4c). The onset of AHE with increasing ν is correlated with a sharp decrease in the transition temperature, consistent with the Kelvin-scale collapse of the symmetry-broken state that gives rise to the hysteresis in Fig. 4a,b. The gradual shift of the transition temperature with increasing ν in Fig. 4, instead of the appearance of a second symmetry breaking transition in the AHE region, supports the notion of a correlated low- T ground state with coupled spin and valley order^{38,39}.

In conclusion, we have observed an AHE, signifying orbital magnetic order, in AB-AB stacked tDBG. The ferromagnetic state occurs only within the strongly interacting ‘halo’ regions of the (ν, D) plane. Strong magnetic anisotropy suggests valley ferromagnetism, while in-plane field signatures indicate a complex interplay of broken spin/valley symmetries in the correlated metallic state of tDBG.

Methods

Device fabrication

High quality AB-AB stacked tDBG devices were fabricated using the ‘modified’ tear and stack technique^{1,40}. First, a large bilayer graphene (BLG) flake $\sim 70 \mu\text{m}$ was exfoliated on a Si/SiO_2 substrate with 285 nm oxide. The BLG flake was mechanically pre-cut into two pieces using a sharp $\sim 1 \mu\text{m}$ diameter tungsten dissecting needle which was attached to the micromanipulator in our transfer setup. Using a stamp made of polybisphenol carbonate (PC) on polydimethylsiloxane (PDMS), the top $h\text{BN}$ layer was picked up at $T = 100^\circ\text{C}$. Next, the BLG flake was picked up at $T = 30^\circ\text{C}$. The stage was rotated to 1.36° , followed by picking up the second BLG at $T = 30^\circ\text{C}$. Then the bottom $h\text{BN}$ layer was picked up at $T = 100^\circ\text{C}$, followed by graphite at $T = 110^\circ\text{C}$. The sequence of stacking from top to bottom is $h\text{BN}$, tDBG, $h\text{BN}$ and graphite. Finally, the entire stack was deposited on a Si/SiO_2 substrate at $T = 175^\circ\text{C}$. Top gate was defined using electron beam lithography (EBL), followed by deposition of Cr/Au (5 nm/50 nm). Edge contacts were formed by etching the stack in CHF_3/O_2 plasma, followed by deposition of Cr/Au (5 nm/80 nm) at a base pressure of $\sim 1 \times 10^{-7}$ mbar. Finally, another step of EBL and etching was done to pattern the device

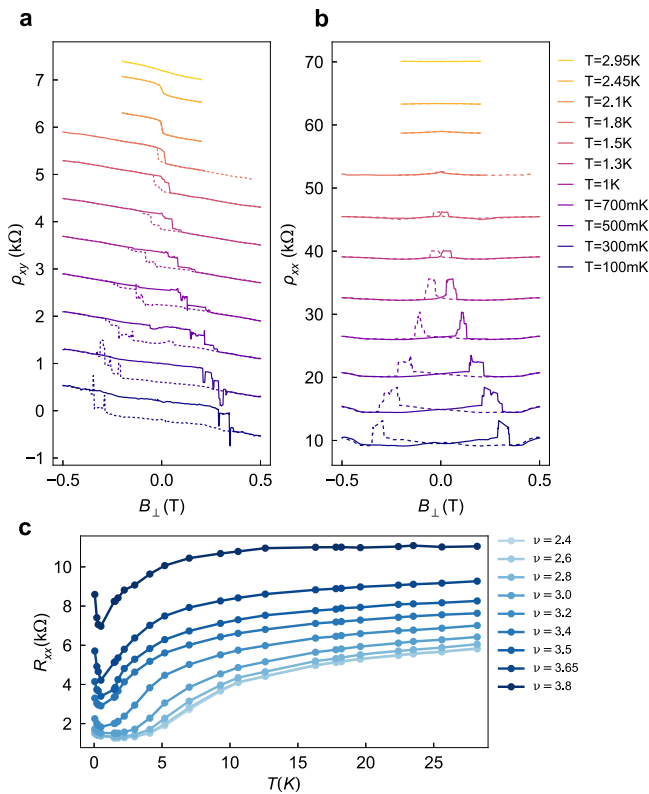


Fig. 4 | Temperature dependence of AHE. a Temperature dependence of hysteretic loop $\rho_{xy}(B_{\perp})$ ($D2, \nu = 3.57, D = -0.43$ V/nm). Curves are offset by 800Ω for clarity. **b** Temperature dependence of $\rho_{xx}(B_{\perp})$; curves offset by $6 \text{ k}\Omega$ for clarity. **c** Temperature dependence $R_{xx}(T)$ at $\mathbf{B} = 0$ in the halo region for ν in the range $\nu = 2.4\text{--}3.8$ ($D1, D = -0.43$ V/nm).

in a Hall bar geometry. The top and bottom *h*BN thickness was determined by atomic force microscope.

Transport measurements

The transport measurements were performed in four terminal configuration, using standard lock in (SRS830) techniques at *f*-13.3 Hz with a current bias *I* = 1 nA. The experiment was carried out in a Bluefors cryogen-free dilution refrigerators equipped with a 3-axis magnet enabling simultaneous control of in- and out-of-plane magnetic fields. Except where noted, measurements were carried out at the nominal base temperature of the refrigerator, with the mixing chamber at 10–15 mK, but heating due to magnetic field sweeps raised the sample temperature up to 50–200 mK depending on sweep conditions.

Twist angle, θ , was calculated from the density corresponding to full filling of the moiré miniband $n(\nu = \pm 4) = 8\theta^2 / \sqrt{3}a^2$, where $a = 0.246$ nm is the lattice constant of graphene. In D1, $\nu = \pm 4$ corresponds $n = \pm 4.05 \times 10^{12} \text{cm}^{-2}$, indicating a twist angle $\theta \approx 1.31^\circ$. In D2, $\nu = \pm 4$ corresponds $n = \pm 4.16 \times 10^{12} \text{cm}^{-2}$ giving $\theta \approx 1.34^\circ$.

Top gate (V_{tg}) and bottom gate (V_{bg}) voltages were used to control the charge carrier density (*n*) and the displacement field (*D*) independently. The density is given by $n = (C_{bg}V_{bg} + C_{tg}V_{tg})/e$ and the displacement field is given by $D = |C_{bg}V_{bg} - C_{tg}V_{tg}|/2\epsilon_0$, where C_{bg} (C_{tg}) are the bottom(top) gate capacitances per unit area, *e* is the electronic charge and ϵ_0 is the vacuum permittivity. We label the field symmetrized (anti-symmetrized) data for R_{xx} (R_{xy}) as ρ_{xx} (ρ_{xy}), where $\rho_{xx}(B, \uparrow) = \frac{R_{xx}(B, \uparrow) + R_{xx}(B, \downarrow)}{2}$, $\rho_{xx}(B, \downarrow) = \frac{R_{xx}(B, \downarrow) + R_{xx}(B, \uparrow)}{2}$ and the anti-symmetrized Hall resistance $\rho_{xy}(B, \uparrow) = \frac{R_{xy}(B, \uparrow) - R_{xy}(B, \downarrow)}{2}$, $\rho_{xy}(B, \downarrow) = \frac{R_{xy}(B, \downarrow) - R_{xy}(B, \uparrow)}{2}$, using \uparrow, \downarrow to indicate the magnetic field sweep direction.

Data availability

Additional information related to this work is available from the corresponding author upon reasonable request. Source data are provided with this paper.

Code availability

The code used for the purposes of analyzing data is also available from the corresponding author upon request.

References

1. Cao, Y. et al. Correlated insulator behaviour at half-filling in magic-angle graphene superlattices. *Nature* **556**, 80 (2018).
2. Cao, Y. et al. Unconventional superconductivity in magic-angle graphene superlattices. *Nature* **556**, 43 (2018).
3. Balents, L., Dean, C. R., Efetov, D. K. & Young, A. F. Superconductivity and strong correlations in moiré flat bands. *Nat. Phys.* **16**, 725 (2020).
4. Andrei, E. Y. & MacDonald, A. H. Graphene bilayers with a twist. *Nat. Mater.* **19**, 1265 (2020).
5. Zhang, Y.-H., Mao, D., Cao, Y., Jarillo-Herrero, P. & Senthil, T. Nearly flat chern bands in moiré superlattices. *Phys. Rev. B* **99**, 075127 (2019).
6. Bistritzer, R. & MacDonald, A. H. Moiré bands in twisted double-layer graphene. *Proc. Natl. Acad. Sci. USA* **108**, 12233 (2011).
7. Zhang, Y., Tan, Y.-W., Stormer, H. L. & Kim, P. Experimental observation of the quantum hall effect and berry’s phase in graphene. *Nature* **438**, 201 (2005).
8. Chittari, B. L., Chen, G., Zhang, Y., Wang, F. & Jung, J. Gate-tunable topological flat bands in trilayer graphene boron-nitride moiré superlattices. *Phys. Rev. Lett.* **122**, 016401 (2019).
9. Koshino, M. Band structure and topological properties of twisted double bilayer graphene. *Phys. Rev. B* **99**, 235406 (2019).
10. Lee, J. Y. et al. Theory of correlated insulating behaviour and spin-triplet superconductivity in twisted double bilayer graphene. *Nat. Commun.* **10**, 1 (2019).
11. Xie, Y. et al. Fractional chern insulators in magic-angle twisted bilayer graphene. *Nature* **600**, 439 (2021).
12. Oh, M. et al. Evidence for unconventional superconductivity in twisted bilayer graphene. *Nature* **600**, 240 (2021).
13. Du, L. et al. Engineering symmetry breaking in 2d layered materials. *Nat. Rev. Phys.* **3**, 193 (2021).
14. Nagaosa, N., Sinova, J., Onoda, S., MacDonald, A. H. & Ong, N. P. Anomalous hall effect. *Rev. Mod. Phys.* **82**, 1539 (2010).
15. Sharpe, A. L. et al. Emergent ferromagnetism near three-quarters filling in twisted bilayer graphene. *Science* **365**, 605 (2019).
16. Serlin, M. et al. Intrinsic quantized anomalous hall effect in a moiré heterostructure. *Science* **367**, 900 (2020).
17. Geisenhof, F. R. et al. Quantum anomalous hall octet driven by orbital magnetism in bilayer graphene. *Nature* **598**, 53 (2021).
18. Chebrolu, N. R., Chittari, B. L. & Jung, J. Flat bands in twisted double bilayer graphene. *Phys. Rev. B* **99**, 235417 (2019).
19. Burg, G. W. et al. Correlated insulating states in twisted double bilayer graphene. *Phys. Rev. Lett.* **123**, 197702 (2019).
20. Liu, J., Ma, Z., Gao, J. & Dai, X. Quantum valley hall effect, orbital magnetism, and anomalous hall effect in twisted multilayer graphene systems. *Phys. Rev. X* **9**, 031021 (2019).
21. Shen, C. et al. Correlated states in twisted double bilayer graphene. *Nat. Phys.* **16**, 520 (2020).
22. Liu, X. et al. Tunable spin-polarized correlated states in twisted double bilayer graphene. *Nature* **583**, 221 (2020).
23. Cao, Y. et al. Tunable correlated states and spin-polarized phases in twisted bilayer-bilayer graphene. *Nature* **583**, 215 (2020).
24. He, M. et al. Symmetry breaking in twisted double bilayer graphene. *Nat. Phys.* **17**, 26 (2021).

25. Wang, Y. et al. Bulk and edge properties of twisted double bilayer graphene. *Nat. Phys.* **18**, 48 (2022).
 26. Sinha, S. et al. Bulk valley transport and berry curvature spreading at the edge of flat bands. *Nat. Commun.* **11**, 1 (2020).
 27. Sinha, S. et al. Berry curvature dipole senses topological transition in a moiré superlattice. *Nat. Phys.* **18**, 765–770 (2022)
 28. Liu, X. et al. Spectroscopy of a tunable moiré system with a correlated and topological flat band. *Nature Comm.* **12**, 1 (2021).
 29. Nomura, K. & MacDonald, A. H. Quantum hall ferromagnetism in graphene. *Phys. Rev. Lett.* **96**, 256602 (2006).
 30. Young, A. F. et al. Spin and valley quantum hall ferromagnetism in graphene. *Nat. Phys.* **8**, 550 (2012).
 31. Liu, J. & Dai, X. Anomalous hall effect, magneto-optical properties, and nonlinear optical properties of twisted graphene systems. *npj Comput. Mater.* **6**, 1 (2020).
 32. Tschirhart, C. et al. Imaging orbital ferromagnetism in a moiré chern insulator. *Science* **372**, 1323 (2021).
 33. Sharpe, A. L. et al. Evidence of orbital ferromagnetism in twisted bilayer graphene aligned to hexagonal boron nitride. *Nano Lett.* **21**, 4299 (2021).
 34. Kim, K. et al. van der waals heterostructures with high accuracy rotational alignment. *Nano Lett.* **16**, 1989 (2016).
 35. Rickhaus, P. et al. Correlated electron-hole state in twisted double-bilayer graphene. *Science* **373**, 1257 (2021).
 36. Sichau, J. et al. Resonance microwave measurements of an intrinsic spin-orbit coupling gap in graphene: A possible indication of a topological state. *Phys. Rev. Lett.* **122**, 046403 (2019).
 37. Lin, J. -X. et al. Spin-orbit-driven ferromagnetism at half moiré filling in magic-angle twisted bilayer graphene. *Science* **375**, 437 (2022)
 38. Kasuya, T. Electrical resistance of ferromagnetic metals. *Prog. Theor. Phys* **16**, 58 (1956).
 39. Petrova, A. E., Bauer, E. D., Krasnorussky, V. & Stishov, S. M. Behavior of the electrical resistivity of MnSi at the ferromagnetic phase transition. *Phys. Rev. B* **74**, 092401 (2006).
 40. Kim, K. et al. Tunable moiré bands and strong correlations in small-twist-angle bilayer graphene. *Proc. Natl. Acad. Sci. USA* **114**, 3364 (2017).
- #941541. A.H.M. was supported by was supported by the U.S. Department of Energy, Office of Science, Basic Energy Sciences, under Awards # DE-SC0019481 and DE-SC0022106. K.W. and T.T. acknowledge support from JSPS KAKENHI (Grant Numbers 19H05790, 20H00354 and 21H05233).

Author contributions

M.K. fabricated the devices, with help from A.V.; M.K., C.C., and Z.G. performed transport measurements and analysed the data; M.K., J.F., J.Z. and A.H.M. interpreted the data; M.K. and J.F. wrote the manuscript. K.W. and T.T. provided the hBN crystals.

Competing interests

The authors declare no competing interests.

Additional information

Supplementary information The online version contains supplementary material available at <https://doi.org/10.1038/s41467-022-34192-x>.

Correspondence and requests for materials should be addressed to Manabendra Kuri or Joshua Folk.

Reprints and permissions information is available at <http://www.nature.com/reprints>

Publisher's note Springer Nature remains neutral with regard to jurisdictional claims in published maps and institutional affiliations.

Open Access This article is licensed under a Creative Commons Attribution 4.0 International License, which permits use, sharing, adaptation, distribution and reproduction in any medium or format, as long as you give appropriate credit to the original author(s) and the source, provide a link to the Creative Commons license, and indicate if changes were made. The images or other third party material in this article are included in the article's Creative Commons license, unless indicated otherwise in a credit line to the material. If material is not included in the article's Creative Commons license and your intended use is not permitted by statutory regulation or exceeds the permitted use, you will need to obtain permission directly from the copyright holder. To view a copy of this license, visit <http://creativecommons.org/licenses/by/4.0/>.

© The Author(s) 2022

Acknowledgements

We thank Leonid Levitov and Marcel Franz for fruitful discussions and comments, and Ruiheng Su for help with figure illustrations. M.K. and C.C. acknowledge postdoctoral research fellowships from Stewart Blusson Quantum Matter Institute, UBC. J.F. acknowledges funding from NSERC, CIFAR, SBQMI, CFI, and ERC Synergy funding for Project